Photoluminescence and excited states dynamics of Tm^{2+}-doped $CsCa(Cl/Br)_3$ and $CsCa(Br/I)_3$ perovskites

Plokker, M. P.; Biner, D. A.; Dusoswa, N.; Dorenbos, P.; Krämer, K. W.; van der Kolk, E.

DOI
10.1088/2515-7639/ac24ed

Publication date
2021

Document Version
Final published version

Published in
JPhys Materials

JPhys Materials

PAPER • OPEN ACCESS

Photoluminescence and excited states dynamics of Tm^{2+}-doped $CsCa(Cl/Br)_3$ and $CsCa(Br/I)_3$ perovskites

To cite this article: M P Plokker *et al* 2021 *J. Phys. Mater.* **4** 045004

IOP Publishing J. Phys. Mater. 4 (2021) 045004 https://doi.org/10.1088/2515-7639/ac24ed

Journal of Physics: Materials

OPEN ACCESS

RECEIVED
19 July 2021

REVISED
18 August 2021

ACCEPTED FOR PUBLICATION
8 September 2021

PUBLISHED
21 September 2021

PAPER

Photoluminescence and excited states dynamics of Tm^{2+}-doped $CsCa(Cl/Br)_3$ and $CsCa(Br/I)_3$ perovskites

M P Plokker[1,*], D A Biner[3], N Dusoswa[2], P Dorenbos[1], K W Krämer[3] and E Van Der Kolk[1]

[1] Department of Radiation Science and Technology, Delft University of Technology, Mekelweg 15, 2629 JB Delft, The Netherlands
[2] Department of Chemical Engineering, Delft University of Technology, Van der Maasweg 9, 2629 HZ Delft, The Netherlands
[3] Department of Chemistry and Biochemistry, University of Bern, Freiestrasse 3, 3012 Bern, Switzerland
[*] Author to whom any correspondence should be addressed.

E-mail: m.p.plokker@tudelft.nl

Keywords: $CsCaCl_3:Tm^{2+}$, $CsCaBr_3:Tm^{2+}$, $CsCaI_3:Tm^{2+}$, Tm^{2+} doped halides, halide solid solutions with Tm^{2+}, Tm^{2+} excited states dynamics, photoluminescence

Supplementary material for this article is available online

Abstract

In this study, we systematically vary the Cl/Br and Br/I ratios in $CsCaX_3:Tm^{2+}$ (X = Cl, Br, I) and hereby gradually shift the positions of the Tm^{2+} $4f^{12}5d^1$-levels as relative to the two $4f^{13}$ levels. At low temperatures up to five distinct Tm^{2+} $4f^{12}5d^1 \rightarrow 4f^{13}$ emissions and the $4f^{13} \rightarrow 4f^{13}$ emission can be observed. As the temperature increases, most of the $4f^{12}5d^1 \rightarrow 4f^{13}$ emissions undergo quenching via multi-phonon relaxation (MPR) and at room temperature only the lowest energy $4f^{12}5d^1 \rightarrow 4f^{13}$ and the $4f^{13} \rightarrow 4f^{13}$ emission remains. For all compositions a $4f^{13} \rightarrow 4f^{13}$ risetime phenomenon is then observed whose duration matches the $4f^{12}5d^1 \rightarrow 4f^{13}$ decay time. It shows the feeding of the $4f^{13}$ state after $4f^{12}5d^1$ excitation. Surprisingly, the feeding time becomes longer from Cl→Br→I, while the related $4f^{12}5d^1$-$4f^{13}$ energy gap becomes smaller. The temperature dependence of the $4f^{12}5d^1 \rightarrow 4f^{13}$ and $4f^{13} \rightarrow 4f^{13}$ emission intensity shows a anticorrelation as earlier observed in other systems and confirms that the feeding process is thermally stimulated. However, the thermally stimulated activation energies that control the feeding process, increase from Cl→Br→I despite our observation that the $4f^{12}5d^1$-$4f^{13}$ energy gap becomes smaller. An analysis reveals that the unexpected behaviour in risetime and activation energy, as a function of composition, cannot be explained by $4f^{12}5d^1 \rightarrow 4f^{13}$ feeding via interband crossing, but more likely via MPR where the electron–phonon coupling strength decreases from Cl→Br→I. No strong relation was found between composition and the quantum efficiency (QE) of the $4f^{13} \rightarrow 4f^{13}$ emission, due to the presence of fluctuations that are likely caused by intrinsic differences in sample quality. Nevertheless, a $4f^{13} \rightarrow 4f^{13}$ QE of up to 70% has been observed and the materials can therefore be used in luminescence solar concentrators.

1. Introduction

In recent years, organolead halide perovskites have received considerable attention in view of photosensitive and optoelectronic applications [1–3]. However, for studying the luminescence properties of lanthanides (Ln), the bandgap of these host compounds is in most cases too small to allow for Ln^{2+} $4f^{12}5d^1 \rightarrow 4f^{13}$ emission [4] and suitable replacements are often found among $CsMX_3$ (M = Ba, Sr, Ca, Mg; X = Cl, Br, I) systems. Recent studies on divalent lanthanides include the works Suta *et al* [5–8] on $CsMX_3:Yb^{2+}$ (M = Sr, Ca; X = Cl, Br, I) and $CsMBr_3:Eu^{2+}$ (M = Sr, Ca, Mg) and those of Lindsey and Loyd *et al* [9–11] on $CsSrBr_3:Eu^{2+}$, $CsCaI_3:Eu^{2+}$ and solid solutions of $CsCa(I/Br)_3:Eu^{2+}$. These materials can be used as scintillators and low energy emitting LEDs [5–11]. For the divalent lanthanide Tm^{2+}, Grimm and Beurer *et al* [12–17] were the first to study its luminescence properties and excited states dynamics in $CsCaX_3$ (X = Cl, Br, I) perovskites, in view of upconversion applications. At low temperature, up to six distinct Tm^{2+} emissions are present: five $4f^{12}5d^1 \rightarrow 4f^{13}$ emissions and the $4f^{13} \rightarrow 4f^{13}$ emission. The quenching of the different

$4f^{12}5d^1 \rightarrow 4f^{13}$ emissions at higher temperature was in each case attributed to multi-phonon relaxation (MPR). The follow-up studies by de Jong *et al* [18, 19] revealed that the relative configurational displacement of the $4f^{12}5d^1(t_{2g})$ states is negligible, which supports the $4f^{12}(5d^1\text{-}5d^1)$ quenching via MPR. Our recent work on $CaX_2:Tm^{2+}$ (X = Cl, Br, I) [20] discloses that the quenching of the lowest energy $4f^{12}5d^1 \rightarrow 4f^{13}$ emission occurs via $4f^{12}5d^1\text{-}4f^{13}$ MPR at low temperatures and predominantly via interband crossing (IC) at the higher temperatures. Therefore, we have decided to reexamine the quenching of this emission in $CsCaX_3:Tm^{2+}$ (X = Cl, Br, I) compounds by systematically varying the Cl/Br and Br/I ratios. This enables us to alter the $4f^{12}5d^1$-level positions relative to the $4f^{13}$-levels, the Stokes shift and the phonon energies. The $4f^{12}5d^1$ tuning by chemical variation allows for a systematic study of the MPR and IC quenching processes as a function of the $4f^{12}5d^1\text{-}4f^{12}5d^1$ and $4f^{12}5d^1\text{-}4f^{13}$ energy gaps. Our temperature-dependent emission and excitation data is compared with the directly measured quantum efficiency (QE) of the $4f^{13} \rightarrow 4f^{13}$ emission. This parameter is ultimately governed by the Tm^{2+} excited states dynamics and determines the suitability of the materials for application in luminescence solar concentrators [21].

In this article we start off with a structural and luminescence characterisation of the $CsCa(Cl/Br)_3:Tm^{2+}$ and $CsCa(Br/I)_3:Tm^{2+}$ samples, subsequently their $4f^{13} \rightarrow 4f^{13}$ QE is determined and we finish with a description of the $4f^{12}(5d^1\text{-}5d^1)$ and $4f^{12}5d^1\text{-}4f^{13}$ quenching processes. We will show that the quenching of the lowest energy Tm^{2+} $4f^{12}5d^1 \rightarrow 4f^{13}$ emission, over temperature, is not straightforwardly explained by a reduced $4f^{12}5d^1\text{-}4f^{13}$ energy gap combined with phonon energies, but more likely governed by the electron–phonon coupling strength.

2. Experimental methods

2.1. Sample synthesis

Nominally 2% Tm^{2+}-doped $CsCa(Cl_{1-y}Br_y)_3$ ($y = 0, 0.25, 0.5, 0.75, 1$) and $CsCa(Br_xI_{1-x})_3$ ($x = 0, 0.2, 0.4, 0.5, 0.6, 0.8, 1.0$) samples were prepared by mixing stoichiometric amounts of CsBr, $CaBr_2$ and TmI_2 with CsCl and $CaCl_2$ or CsI and CaI_2 respectively. A small amount of Tm metal was added to prohibit any oxidation of Tm^{2+} towards Tm^{3+}. The powder mixtures were sealed in a tantalum ampoule by arc welding under 0.4 bar helium. The Ta ampoules were subsequently enclosed in a silica ampoule under vacuum and heated in a Carbolite RHF1600 chamber furnace (Carbolite Gero, Neuhausen, Germany) to 800 °C for 20 h. After cooling back to room temperature, the obtained crystalline products were grinded to powder. All handling of starting materials and the final products was done under strictly inert and dry conditions in a glovebox (MBraun, Garching, Germany).

2.2. Sample characterisation

The crystal structures of the samples at room temperature were investigated by powder x-ray diffraction using a STOE Stadi P diffractometer (Stoe & Cie GmbH, Darmstadt, Germany) with Bragg–Brentano geometry and $CuK_{\alpha 1}$ radiation. The lattice parameters were determined from Rietveld refinements using the Fullprof software [22]. Room temperature near-infrared (NIR) absorption measurements were recorded with a Cary 6000i spectrophotometer (Varian Inc., Palo Alto, California) to confirm the absence of Tm^{3+} in the samples. The absorption spectra were measured in transmission from KBr pellets in gas-tight sample cells with silica windows. A part of the powder samples was mixed with KBr and pressed into a pellet under inert conditions.

Luminescence QE measurements were performed at room temperature using an Edinburgh FLS980 spectrometer (Edinburgh Instruments, Livingston, UK) containing an integrating sphere, 450 W xenon arc lamp, and Hamamatsu C9940-02 NIR-photomultiplier tube (PMT) (Hamamatsu Photonics, Hamamatsu, Japan). Highly reflecting BaSO4 and the un-doped host materials were used as reference samples.

Room temperature time resolved measurements were carried out using a tunable EKSPLA NT230 laser (EKSPLA, Vilnius, Lithuania) with a pulse duration of 7 ns. A DT5724F (0–2 ms) or DT5730 (0–40 ms) CAEN digitiser (CAEN, Viareggio, Italy) measured the signal from a H1033A-75 NIR-PMT or a Hamamatsu R7600U-20HV-800 V PMT (Hamamatsu Photonics, Hamamatsu, Japan). Decay signals from a 1000 laser pulses were accumulated for each decay spectrum.

2.3. Temperature-dependent measurements

The temperature dependent excitation and emission spectra were obtained with help of a xenon lamp coupled to a double monochromator with three sets of gratings (UV/VIS/NIR) and a R7600U-20HV-800 V PMT, H1033A-75 NIR-PMT, or C9100-13 EM-CCD (all Hamamatsu Photonics, Hamamatsu, Japan) which were in turn attached to a single monochromator with three different gratings. A calibrated EPLAB NBS 1000 W quartz iodine lamp was used to acquire the wavelength dependent sensitivity of the detectors. The detection ranges were 400–1150 nm and 950–1600 nm for configurational coordinate diagram (CCD) and NIR-PMT, respectively. The spectral overlap allows to couple the output of both detectors and hence

accurately determine the $4f^{12}5d^1 \rightarrow 4f^{13}$ and $4f^{13} \rightarrow 4f^{13}$ emission ratios over temperature. For samples that have no clear emission in the overlap region, a small amount of $Ca_2Si_5N_8$:Yb^{3+} was added to the samples. After exciting the Yb^{3+} at 360 nm, the $^2F_{5/2} \rightarrow {}^2F_{7/2}$ emission at 985 nm was observed and used for scaling the emission spectra recorded with the two detectors. The samples were thermalised by an APD Cryogenic Helium cooler (APD Cryogenics, Allentown Pennsylvania, USA) and a Lakeshore temperature controller (Lakeshore Cryotronics, Westerville Ohio, USA).

Special sample holders were used for the hygroscopic materials during all measurements to prevent unwanted hydration or oxidation reactions [23].

3. Results and discussion

3.1. Sample characterisation

Figure 1 shows the powder x-ray diffraction patterns of the $CsCa(Cl/Br)_3$ and $CsCa(Br/I)_3$:2% Tm^{2+} samples. The lattice parameters, molar volume, and space group of the samples are summarised in table 1. The evaluation of the diffraction patterns reveals that all $CsCa(Cl/Br)_3$ samples and the $CsCa(Br/I)_3$ samples up to the composition $CsCaBr_{1.5}I_{1.5}$ adopt the cubic perovskite structure ($CaTiO_3$ structure) with space group $Pm\bar{3}m$, see figure 2. This is in accordance to the work of Grimm *et al* on $CsCaX_3$:Tm^{2+} (X = Cl, Br, I) [12, 13] and structure reports on $CsCaCl_3$ [24] and $CsCaBr_3$ [25]. The Tm^{2+} ions have an octahedral coordination and randomly replace the Ca^{2+} ions on site (1a) with point symmetry O_h. Along the series Cl→Br→I, the diffraction peaks shift to slightly smaller 2θ values, see figure 1, and the lattice parameter increases. The molar volume increases linearly in good agreement with Vegard's rule. The values are reported in table 1 and displayed in figure S1 of the supplementary information (SI) (available online at stacks.iop.org/JPMATER/4/045004/mmedia).

For higher I content the crystal structures change in accordance with the well-known sequence of perovskite structures. $CsCaBr_{1.2}I_{1.8}$ and $CsCaBr_{0.6}I_{2.4}$ crystallise in the tetragonal $NaNbO_3$ structure with spacegroup $P4/mbm$, which was previously reported for e.g. $CsTmBr_3$ [26] and $CsDyBr_3$ [27]. The CaX_6 octahedra rotate around the *c*-axis to decrease the volume and accommodate the smaller M/X ratio, see figure 2(b). Tm^{2+} ions on site (2a) have C_{4h} site symmetry.

Finally, $CsCaI_3$ adopts the orthorhombic $GdFeO_3$ structure with space group *Pbnm*, where the octahedra are rotated and titled, see figure 2(c). The point symmetry of the Tm^{2+} ions on site (4b) is reduced to C_i. The crystal structure of $CsDyI_3$ was previously determined [27] and lattice parameters of $CsCaI_3$ were reported by Schilling and Meyer [28], who discussed the stability ranges of the ternary AMX_3 phases for X = Br and I.

The Tm^{2+} ions in the $CsCaX_3$ structures occupy the octahedral Ca^{2+}-sites with decreasing symmetry along the $CaTiO_3 \rightarrow NaNbO_3 \rightarrow GdFeO_3$ series, as discussed above. Additionally, the random halide mixture Cl/Br or Br/I slightly distorts the individual Tm^{2+} coordination, which can further split the 5d crystal field levels t_{2g} and e_g. In this work, we use the short hand notation $(^{2S+1}L_J,t_{2g})_S$ to assign the excited $4f^{12}5d^1$ levels, where $^{2S+1}L_J$ represents the state of $4f^{12}$ configuration, t_{2g} denotes the 5d-electron in a level originating from the triplet of the octahedral crystal field splitting, and the subscript *S* denotes the total electron spin of the $(4f^{12} + 5d^1)$ excited state.

The NIR absorption spectra of the $CsCa(Cl/Br)_3$:Tm^{2+} and $CsCa(Br/I)_3$:Tm^{2+} samples are displayed in figure 3. The spectra reveal the presence of the characteristic Tm^{2+} $^2F_{7/2} \rightarrow {}^2F_{5/2}$ absorption near 1140 nm. The spectra do not show any signs of the distinct Tm^{3+} $^3H_6 \rightarrow {}^3H_5$ absorption, which is typically observed at around 1230 nm [20, 29–31]. The samples thus only contain divalent Tm. The integrated values of the Tm^{2+} absorption peak show a deviation of ±7% from average, indicating that the Tm^{2+} doping percentages of the samples are quite close.

The Tm^{2+} $^2F_{5/2}$ and $^2F_{7/2}$ states arising from the $(4f)^{13}$ electron configuration are split by the crystal field into $(2J + 1)/2$ Kramers doublets. Therefore, the $^2F_{7/2} \rightarrow {}^2F_{5/2}$ absorption peak comprises of multiple sharp absorption lines as can be observed in the inset of figure 3. As Tm^{2+} is octahedrally coordinated in each of the samples, the absorption pattern is largely the same. Minor differences are likely caused by differences in the distribution of Cl^-, Br^- and I^- ions around Tm^{2+} and shifts in the interatomic distances due to different crystal structures. For a more-detailed analysis of the Stark splitting in $CsCaX_3$:Tm^{2+} (X = Cl, Br, I), the reader is referred to the works of Grimm *et al* [13, 15].

3.2. Emission and excitation spectra

Figure 4 shows the excitation spectra as acquired on the Tm^{2+} $^2F_{5/2} \rightarrow {}^2F_{7/2}$ emission at 300 K. For the $CsCaX_3$:Tm^{2+} (X = Cl, Br, I) samples, the spectra are similar in shape to the 20 K UV/NIR/VIS absorption spectra reported before by Grimm *et al* [13, 15, 17]. The provided classification of the lowest energetic 5d-levels is added to figure 4 and their positioning is shown for $CsCaCl_3$:Tm^{2+} by the vertical dashed lines. As can faintly be seen, the spin-forbidden $(^3H_6,t_{2g})_{S=3/2}$ levels are located at around 750–800 nm and

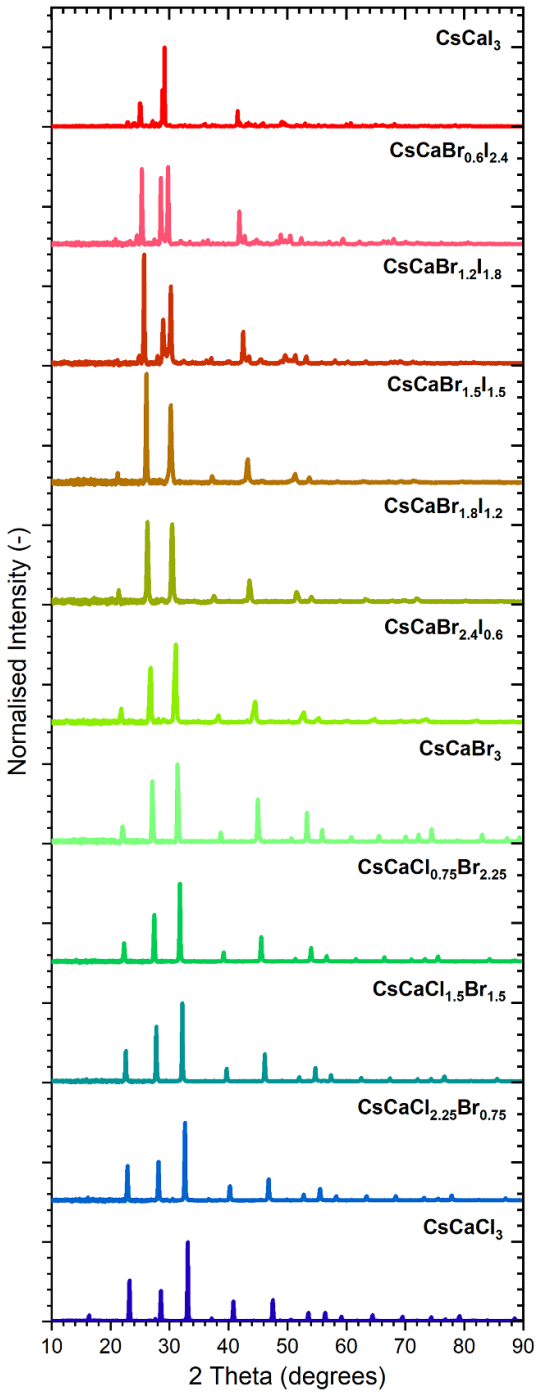

Figure 1. Powder x-ray diffraction patterns of the $CsCa(Cl/Br)_3:Tm^{2+}$ and $CsCa(Br/I)_3:Tm^{2+}$ samples at room temperature. The corresponding crystallographic data is summarised in table 1.

positioned in the tail of the broad spin-allowed $(^3H_6,t_{2g})_{S=1/2}$ levels. The excitation spectra acquired on the $(^3H_6,t_{2g})_{S=3/2}\rightarrow{}^2F_{7/2}$ emission at 20 K are displayed in figure 5 and provide a much clearer sighting of the spin-forbidden $(^3H_6,t_{2g})_{S=3/2}$ levels. In addition, a second set of $(^3H_6,t_{2g})_{S=3/2}$ levels can be distinguished at around 620 nm. It is located in between the less broad $(^3H_6,t_{2g})_{S=1/2}$ levels. This was also the case in our recent work on $CaX_2:Tm^{2+}$ (X = Cl, Br, I) [20]. Near the end of section 3.4 we will discuss the differences between the $^2F_{5/2}\rightarrow{}^2F_{7/2}$ and $(^3H_6,t_{2g})_{S=3/2}\rightarrow{}^2F_{7/2}$ excitation spectra into more detail.

A mutual comparison between the $CsCaX_3:Tm^{2+}$ (X = Cl, Br, I) spectra shows that the $4f^{12}5d^1$ levels undergo a redshift upon traversing from Cl→Br→I. In particular, the $(^3H_6,t_{2g})_{S=1/2}$ levels shift by around 240 cm^{-1} for Cl→Br and approximately 920 cm^{-1} in case of Br→I. It indicates a decrease of the centroid shift along the series. This is expected based on a decrease in the average bonding strength between anion and cation following the nephelauxetic sequence: Cl→Br→I [32]. In addition to that, figures S1 and S2 in the

Table 1. Composition, space group, lattice parameters, and molar volume of the $CsCa(Cl/Br)_3$ and $CsCa(Br/I)_3$:2%Tm^{2+} samples.

Sample	Space group	*a*/Å	*b*/Å	*c*/Å	V/(cm^3 mol^{-1})
$CsCaCl_3$	$Pm\bar{3}m$ (no. 221)	5.40351(9)	—	—	95.025(3)
$CsCaCl_{2.25}Br_{0.75}$	$Pm\bar{3}m$	5.48002(14)	—	—	99.119(4)
$CsCaCl_{1.5}Br_{1.5}$	$Pm\bar{3}m$	5.55293(13)	—	—	103.129(4)
$CsCaCl_{0.75}Br_{2.25}$	$Pm\bar{3}m$	5.62403(15)	—	—	107.141(5)
$CsCaBr_3$	$Pm\bar{3}m$	5.69583(12)	—	—	111.297(4)
$CsCaBr_{2.4}I_{0.6}$	$Pm\bar{3}m$	5.7622(4)	—	—	115.232(15)
$CsCaBr_{1.8}I_{1.2}$	$Pm\bar{3}m$	5.8647(5)	—	—	121.492(16)
$CsCaBr_{1.5}I_{1.5}$	$Pm\bar{3}m$	5.9078(5)	—	—	124.19(2)
$CsCaBr_{1.2}I_{1.8}$	$P4/mbm$ (no. 127)	8.2608(8)	—	6.0899(5)	125.13(2)
$CsCaBr_{0.6}I_{2.4}$	$P4/mbm$	8.3991(7)	—	6.1822(5)	131.339(18)
$CsCaI_3$	$Pbnm$ (no. 62)	8.5540(5)	8.6237(5)	12.2885(7)	136.495(13)

SI reveal an increase in the molar volume and lattice parameters for Cl→Br→I, leading to a decrease in the centroid shift and increase in the crystal field splitting along the series [32, 33].

Figure 2 already showed that, as the Cl/Br and Br/I ratios in the $CsCaX_3$:Tm^{2+} (X = Cl, Br, I) samples are adjusted, the anion coordination around Tm^{2+} remains octahedral and six-fold. The different anion species (Cl, Br, I) will be distributed randomly over the anion positions of the coordination polyhedra. This random distribution will result in many different anion surroundings for each individual Tm^{2+} ion with corresponding changes in size of the coordination polyhedra. The mixed compounds will thus have slightly different values for the centroid shift and crystal field splitting.

Figure 6 displays the emission spectra of the samples after excitation into the $(^3F_4,t_{2g})_{S=1/2}$ levels. The full coloured curves were acquired at 20 K and reveal up to six distinct Tm^{2+} emissions: five $4f^{-1}{}^2 5d^1 \rightarrow 4f^{13}$ emissions (B, C, D, E, F) and the $4f^{13} \rightarrow 4f^{13}$ emission (A). These emissions are labelled according to the classification introduced by Grimm and Beurer *et al* [12–14]. A schematic overview of the transitions and their lettering is provided in figure 7. As the temperature increases, most of the $4f^{12}5d^1 \rightarrow 4f^{13}$ emissions (B, C, D, E, F) will quench and are no longer observed. This can be seen in the softly coloured emission spectra, that were acquired at 300 K and which are plotted alongside the 20 K spectra. $CsCaI_3$:Tm^{2+} forms a special case where emissions A, B, C, and D are still, albeit weakly, present at 300 K. It will be discussed in more detail in section 3.4. For all studied compounds, however, emission B survives as the most intense $4f^{12}5d^1 \rightarrow 4f^{13}$ emission at 300 K, while the $4f^{13} \rightarrow 4f^{13}$ emission A has become the most dominant emission of all.

When traversing from Cl→Br→I, the dashed lines in figure 6 show that the emissions undergo a gradual shift towards longer wavelengths. The shifts in the related excitation levels is visualised by similar dashed lines in figure 5. Note that for all compounds, Tm^{2+} is octahedrally coordinated and the shift is related to nephelauxetic effects. Tables S1 and S2 in the SI provide an overview of the emission and excitation level positioning and characterises their shift as a function of composition. Based on these values, the energy gaps between the levels can be calculated. This provides important information for the quenching of the emissions as will be discussed in section 3.4. Furthermore, the close-ups presented in figures S3–S5 in the SI reveal that not all of the emissions are observed in every studied compound. For $CsCaCl_3$:Tm^{2+} only emissions A, B and D are present at 20 K. The study by de Jong *et al* [19] showed that the absence of emission C can be attributed to efficient MPR since the gap between the $(^3H_6,t_{2g})_{S=1/2}$ and $(^3H_6,t_{2g})_{S=3/2}$ levels amounts to less than five times the maximum phonon energy. As the Br/Cl ratio is gradually increased, emission C abruptly emerges in $CsCaCl_{0.75}Br_{2.25}$:Tm^{2+} and intensifies in $CsCaBr_3$:Tm^{2+}. In this latter compound, four emissions are observed at 20 K: A, B, C, and D. When the bromide anions are gradually substituted for iodide, the number of observed emissions still remains the same. Besides, emission B remains the most intense emission at 20 K. However, in $CsCaI_3$:Tm^{2+}, emissions E and F suddenly appear and emission D emerges as the most dominant emission at 20 K. Up to now emission F has only been reported in $CsCaI_3$:Tm^{2+} [14, 17]. Its absence in $CsCaCl_3$:Tm^{2+} and $CsCaBr_3$:Tm^{2+} might be related to the close proximity of neighbouring levels in combination with relatively higher phonon energies as compared to $CsCaI_3$:Tm^{2+}. Emission E was previously also observed in $CsCaCl_3$:Tm^{2+} and $CsCaBr_3$:Tm^{2+} [12, 13]. The reason for its absence in our low temperature spectra is not clear. Since the $(^3F_4,t_{2g})_{S=3/2}$ state has $J = 9/2$ and the $^2F_{5/2}$ state $J = 5/2$, it is forbidden by the $\Delta J = 1$ or 0 selection rule and will therefore appear very weak in intensity. Furthermore, the much larger energy gap between the $(^3F_4,t_{2g})_{S=3/2}$ and $(^3H_6,t_{2g})_{s=1/2}$ levels in $CsCaI_3$:Tm^{2+} combined with lower phonon energies will prolong an immediate quenching via MPR, as might be the case for $CsCaCl_3$:Tm^{2+} and $CsCaBr_3$:Tm^{2+}.

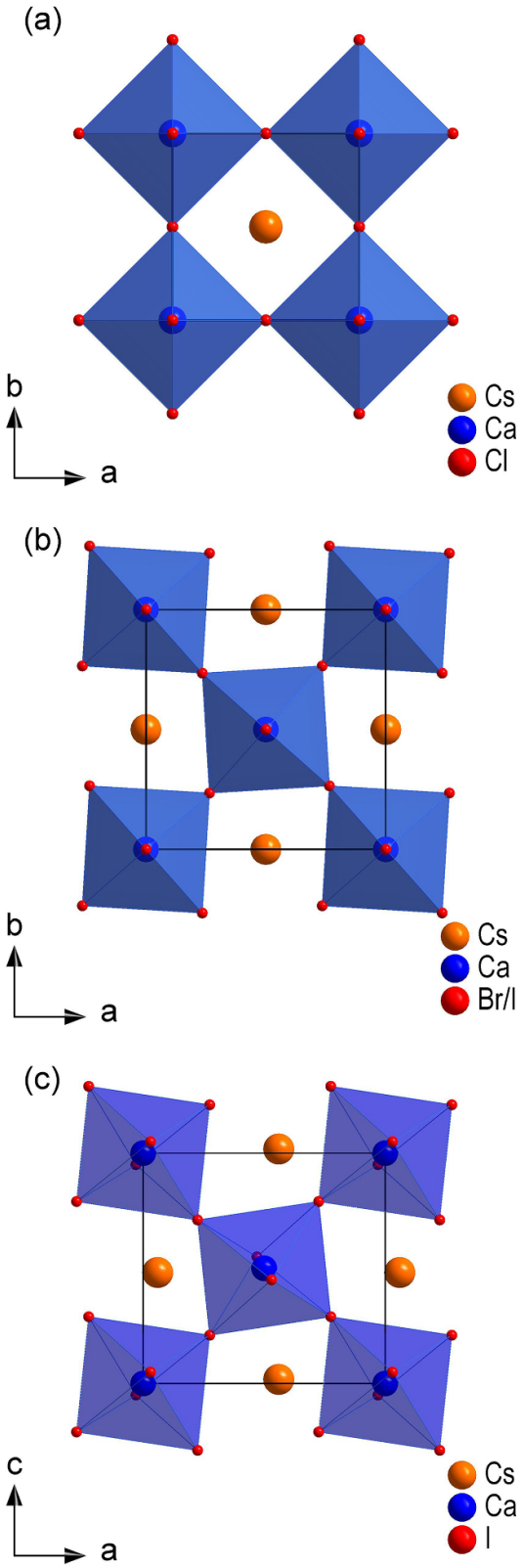

Figure 2. Crystal structures of (a) $CsCaCl_3$, (b) $CsCaBr_{1.2}I_{1.8}$, and (c) $CsCaI_3$ that respectively adopt the structures of $CaTiO_3$, $NaNbO_3$, and $GdFeO_3$ type perovskites.

3.3. Luminescence QE

For each of the $CsCa(Cl/Br)_3:Tm^{2+}$ and $CsCa(Br/I)_3:Tm^{2+}$ samples, the internal QE of $^2F_{5/2}\rightarrow{}^2F_{7/2}$ emission A was determined after excitation into the lower energy $(^3H_6,t_{2g})_{S=1/2}$ levels. The obtained values are listed in table S3 of the SI and are plotted versus the Br/Cl and Br/I ratios in red in figure 8. For the $CsCa(Br/I)_3:Tm^{2+}$ samples, the room temperature presence of the $(^3H_6,t_{2g})_{S=3/2}\rightarrow{}^2F_{7/2}$ emission B allows it to determine its QE. These values are displayed in blue.

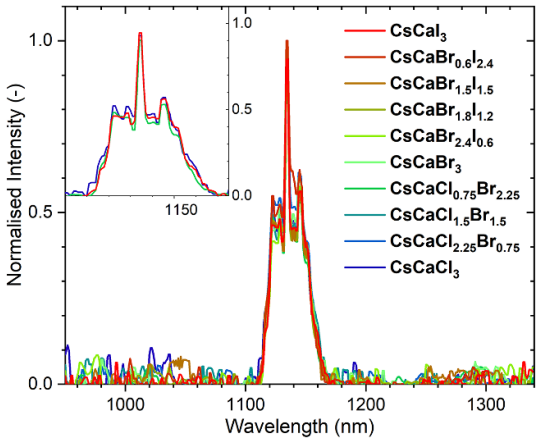

Figure 3. Room temperature NIR absorption spectra of the $CsCa(Cl/Br)_3:Tm^{2+}$ and $CsCa(Br/I)_3:Tm^{2+}$ samples. The Tm^{2+} $^2F_{7/2}\rightarrow{}^2F_{5/2}$ absorption is observed at 1140 nm. No Tm^{3+} $^3H_6\rightarrow{}^3H_5$ absorption is seen at around 1230 nm. The inset shows a close-up of the $CsCaX_3:Tm^{2+}$ spectra for X = Cl, Br, I.

When adding up the QE contributions of emission A and B, the overall QE value ranges from 40% to 70%. However, it appears that the QE values of emission A in the mixed compounds undergo fluctuations with composition. These fluctuations were reproduced by a second independent measurement on another badge of the same sample, see the orange data points. The absorption, as displayed in black and grey, on the other hand stays almost constant over the entire sample series. This was also observed in the $4f^{13}\rightarrow4f^{13}$ absorption spectra back in figure 3. As the fluctuations do not have a correlation with composition and are not caused by measurement mistakes or sample degradation, we believe they are more likely related to intrinsic sample differences such as perhaps different defect densities. The large fluctuations prevent us to draw any conclusions on the QE of emission A for the $CsCa(Cl/Br)_3:Tm^{2+}$ sample series. Nevertheless, we are able to recognise a clear trend for the $CsCa(Br/I)_3:Tm^{2+}$ sample series. From $CsCaBr_{2.4}I_{0.6}:Tm^{2+}$ onwards, the QE of emission A decreases rapidly from around 70% to a mere value of around 15% at $CsCaI_3:Tm^{2+}$. In the same interval, the QE of emission B increases from around 7% to 45% and displays an anti-correlated trend with respect to emission A. This feature was examined further by the room temperature decay curves presented in figure 9. Upon gradually traversing from Cl→Br→I, the decay curves related to emission B lengthen and the luminescence lifetime increases. The decay curves related to emission A, on the other hand, display a clear risetime due to a feeding phenomenon as measured and numerically modelled by us before [20, 30, 31]. Counter intuitively, it is observed that the risetime increases from Cl→Br→I, while the energy gap between the $(^3H_6,t_{2g})_{S=3/2}$ and $^2F_{5/2}$ levels decreases. This signifies a slower feeding rate. The inset shows that the lifetime of emission B and observed risetime for emission A are close in values for each of the compositions. It indicates that at room temperature there is a direct feeding from the $(^3H_6,t_{2g})_{S=3/2}$ to the $^2F_{5/2}$ levels, which was also concluded in our study on $CaX_2:Tm^{2+}$ (X = Cl, Br, I) [9]. This explains the reversed trend in the anti-correlated behaviour of their QEs, as shown in figure 8. In the next section, we will study the quenching of the various Tm^{2+} emissions in $CsCaI_3:Tm^{2+}$ and zoom-in on the quenching mechanism of emission B and the feeding of the $^2F_{5/2}$ levels.

3.4. Temperature-dependent luminescence

Since all of the observed emissions (A–F) are present in $CsCaI_3:Tm^{2+}$, we have decided to select this compound for a more detailed study on the luminescence quenching. This also allows it to disclose why, in this compound, emission D is much stronger than emission B.

Figure 10 shows a 3D-plot of the emission spectra versus temperature, as acquired after excitation into the $(^3F_4,t_{2g})_{S=1/2}$ levels. The spectra at 20 K and 300 K were previously presented in figure 6. The inset provides additional quantitative information on the luminescence behaviour. The excited-state absorption studies of de Jong *et al* [7, 8] revealed that for $CsCaCl_3:Tm^{2+}$ and $CsCaBr_3:Tm^{2+}$, the configurational coordinate displacement between the different $4f^{12}5d^1(t_{2g})$ states is negligible. Although such thorough information is missing for $CsCaI_3:Tm^{2+}$, we will assume that this displacement is also very small and that the $4f^{12}5d^1$-$4f^{12}5d^1$ quenching is therefore favoured by MPR. As becomes apparent, $(^3F_4,t_{2g})_{S=1/2}\rightarrow{}^2F_{7/2}$ emission F already starts to quench at 20 K. The temperature-dependent emission spectra in figure S6 in the SI show that at 130 K it can no longer be perceived and has quenched completely.

Both $(^3F_4,t_{2g})_{S=3/2}\rightarrow{}^2F_{7/2}$ emission D and $(^3F_4,t_{2g})_{S=3/2}\rightarrow{}^2F_{5/2}$ emission E emerge from the lowest energy $(^3F_4,t_{2g})_{S=3/2}$ level and will therefore have a similar temperature dependence. The energy gap between

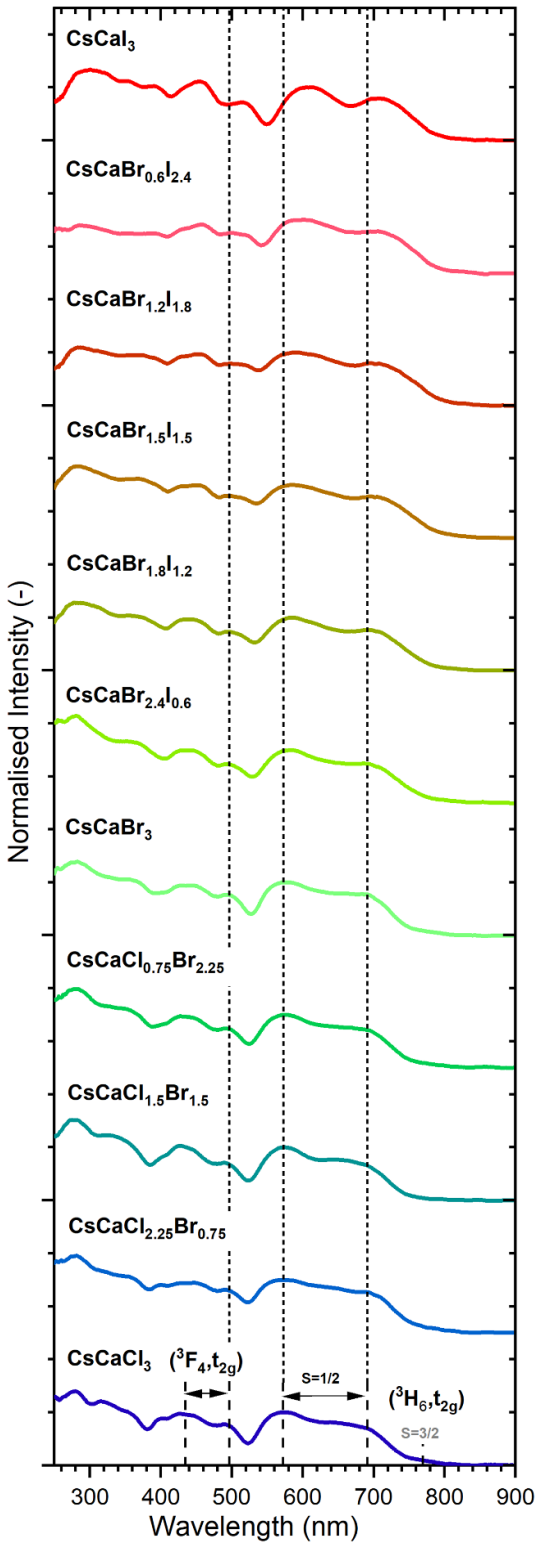

Figure 4. Excitation spectra of the $CsCa(Cl/Br)_3:Tm^{2+}$ and $CsCa(Br/I)_3:Tm^{2+}$ samples as acquired on $^2F_{5/2}\rightarrow{}^2F_{7/2}$ emission A at 300 K. The lowest energy $4f^{12}5d^1$-levels are indicated for $CsCaCl_3:Tm^{2+}$ and undergo a shift towards longer wavelengths upon traversing from Cl→Br→I.

the $(^3F_4,t_{2g})_{S=3/2}$ and $(^3H_6,t_{2g})_{s=1/2}$ levels is around 3025 cm^{-1} or 18 vibrational quanta. For $CsCaCl_3:Tm^{2+}$ and $CsCaBr_3:Tm^{2+}$, the gap between the $(^3F_4,t_{2g})_{S=3/2}$ and $(^3H_6,t_{2g})_{s=1/2}$ levels is of similar size to $CsCaI_3:Tm^{2+}$ and respectively amounts to around 3020 cm^{-1} and 2960 cm^{-1}. However, the required amount of vibrational quanta to bridge it is smaller and respectively resembles 10 and 14 quanta. This might explain why, at low temperature, emission D is more intense in $CsCaI_3:Tm^{2+}$ as compared to $CsCaCl_3:Tm^{2+}$ and $CsCaBr_3:Tm^{2+}$. Besides, in $CsCaI_3:Tm^{2+}$, the energy gap between the $(^3F_4,t_{2g})_{S=3/2}$ and $(^3H_6,t_{2g})_{s=1/2}$

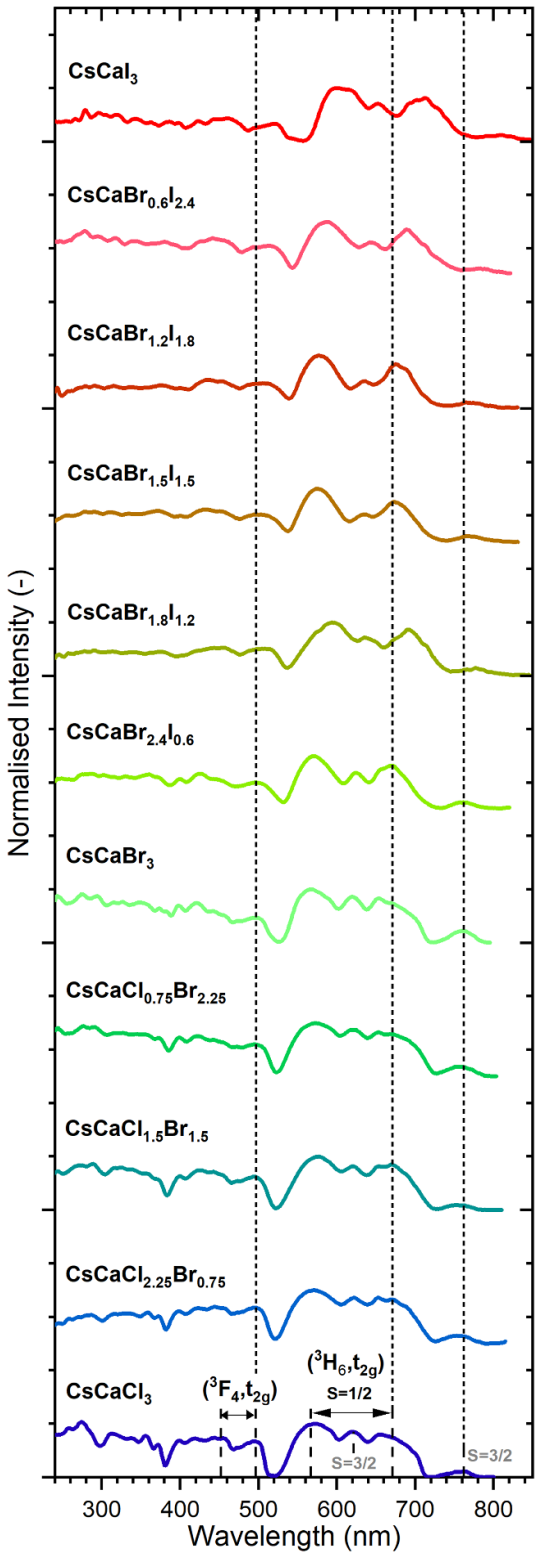

Figure 5. Excitation spectra of the $CsCa(Cl/Br)_3:Tm^{2+}$ and $CsCa(Br/I)_3:Tm^{2+}$ samples as acquired on the Tm^{2+} $(^3H_6,t_{2g})_{S=3/2}\rightarrow{}^2F_{7/2}$ emission B at 20 K. As compared to figure 4, the spin-forbidden $(^3H_6,t_{2g})_{S=3/2}$ levels can be distinguished more clearly.

levels is larger than the gap between the $(^3H_6,t_{2g})_{s=3/2}$ and $^2F_{5/2}$ levels, which is close to 2560 cm^{-1}. This is opposed to $CsCaCl_3:Tm^{2+}$ and $CsCaBr_3:Tm^{2+}$ where the former gap is smaller than the latter. It explains why emission D remains present up to 320 K and why at low temperature it is much more dominant as compared to emission B. A much similar, peculiar, situation was recently encountered by us in when comparing the temperature-dependent luminescence of $CaCl_2:Tm^{2+}$, $CaBr_2:Tm^{2+}$ and $CaI_2:Tm^{2+}$ [20].

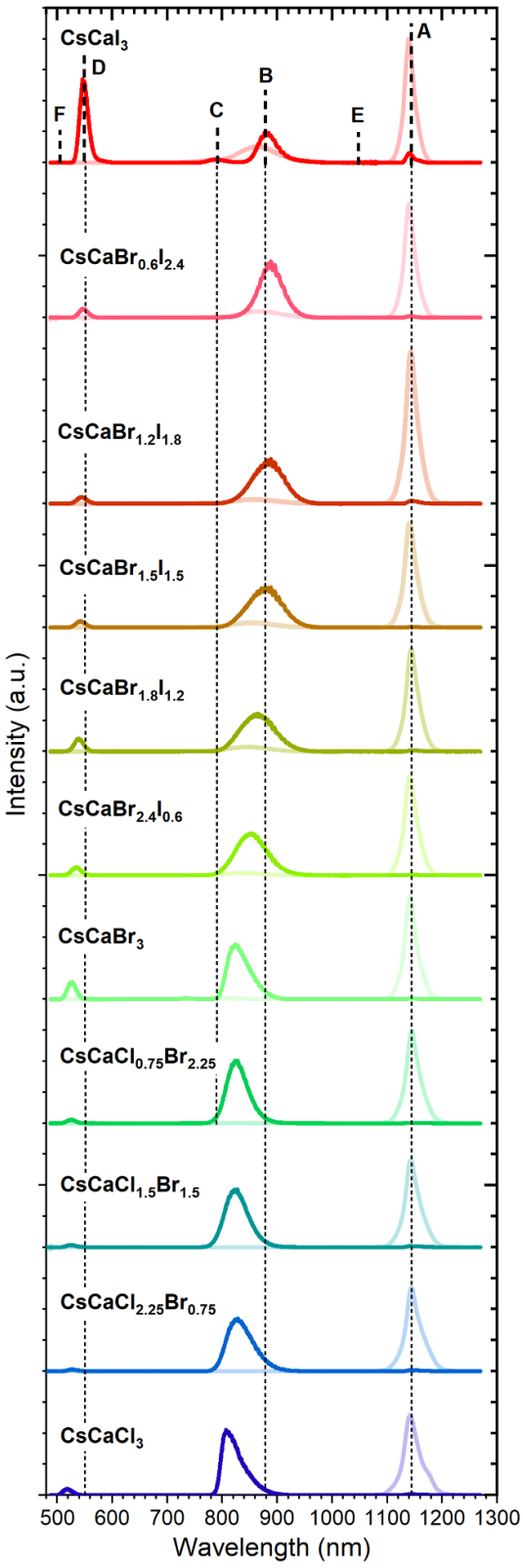

Figure 6. Emission spectra of the $CsCa(Cl/Br)_3:Tm^{2+}$ and $CsCa(Br/I)_3:Tm^{2+}$ samples as obtained after excitation into the $(^3F_4,t_{2g})_{S=1/2}$ levels. The full coloured curves represent the spectra at 20 K, while the softly coloured ones were made at 300 K. The spectra are corrected for the sensitivity of detection and scaled on the measured QE of $^2F_{5/2}\rightarrow{}^2F_{7/2}$ emission A at room temperature.

As emission D quenches, it will feed the lower lying $(^3H_6,t_{2g})_{s=1/2}$ levels from which $(^3H_6,t_{2g})_{S=1/2}\rightarrow{}^2F_{7/2}$ emission C occurs. As the energy gap between the $(^3H_6,t_{2g})_{S=1/2}$ and $(^3H_6,t_{2g})_{S=3/2}$ levels amounts to 1360 cm^{-1} and resembles only eight vibrational quanta, emission C will quench already at very low temperatures and will feed the $(^3H_6,t_{2g})_{S=3/2}$ levels. However, the feeding from the $(^3F_4,t_{2g})_{S=3/2}$ levels, as

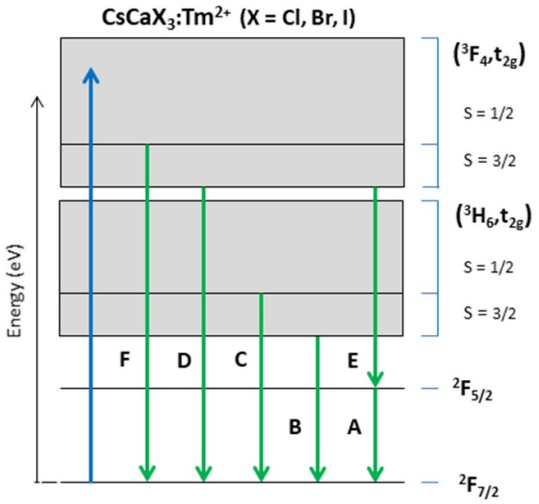

Figure 7. Schematic energy level diagram for the $CsCa(Cl/Br)_3:Tm^{2+}$ and $CsCa(Br/I)_3:Tm^{2+}$ samples at 20 K and after exciting into the $(^3F_4,t_{2g})_{S=1/2}$ levels. The six distinct Tm^{2+} emissions are labelled from A to F.

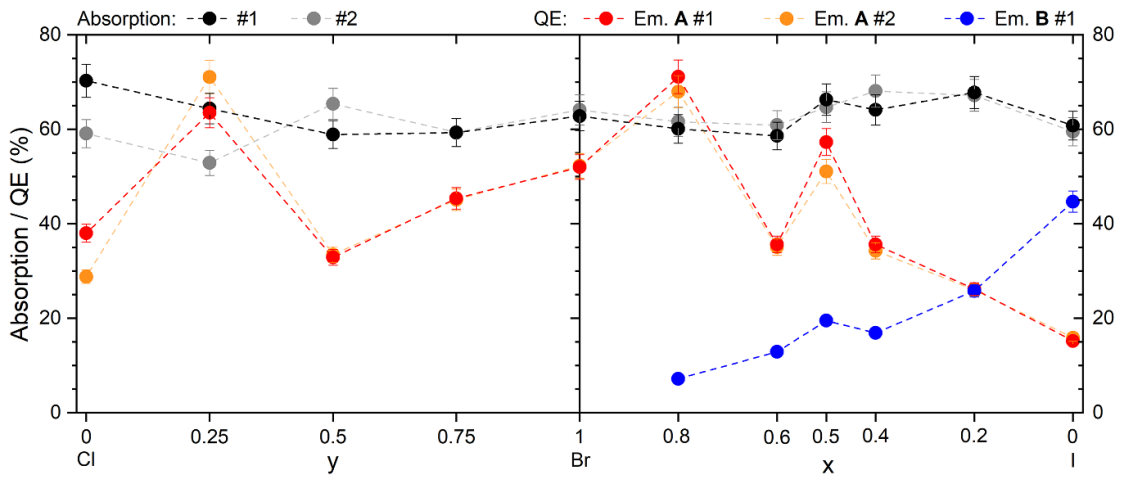

Figure 8. Quantum efficiency of the $^2F_{5/2}\rightarrow{}^2F_{7/2}$ emission A (red) and absorption (black) plotted versus the Br/Cl and Br/I ratio in the samples. For the $CsCa(Br/I)_3:Tm^{2+}$ samples, the QE of $(^3H_6,t_{2g})_{S=3/2}\rightarrow{}^2F_{7/2}$ emission B could also be determined (blue). Photoexcitation occurred at room temperature into the $(^3H_6,t_{2g})_{S=1/2}$ levels. The fluctuation among the QE data points was reproduced by a second independent measurement (orange). The absorption remained the same (grey).

caused by the quenching of emission D, results in its presence even at room temperature. Evidence for this is provided in the temperature-dependent emission spectra in figure S7 in the SI. In addition to that, the inset in figure 10 reveals a decreasing intensity trend for emission C up to 40 K and a sudden increase in intensity as emission D grows weaker.

From the $(^3H_6,t_{2g})_{S=3/2}$ levels emission B occurs. The inset in figure 10 displays a downward intensity trend for this emission at temperatures below 40 K. From 40 K onwards, however, it starts to increase firmly up to a temperature of 260 K. This abrupt increase in intensity indicates a sequential feeding route from $(^3F_4,t_{2g})_{S=3/2}\rightarrow(^3H_6,t_{2g})_{S=1/2}\rightarrow(^3H_6,t_{2g})_{S=3/2}$. Above 260 K the intensity of emission B decreases again, while that of emission A increases most strongly. The energy gap between the $(^3H_6,t_{2g})_{S=3/2}$ and $^2F_{5/2}$ levels resembles around 2560 cm^{-1}, or 15 vibrational quanta. However, since this quenching involves a $4f^{12}5d^1\rightarrow4f^{13}$ relaxation, the quenching might not necessarily occur via MPR. In the next subsection we will further investigate the quenching of emission B. To ease the analysis we will excite directly into the lower energy $(^3H_6,t_{2g})_{s=1/2}$ levels, which allows us to solely monitor the luminescence intensities of emissions A, B and C.

3.4.1. Quenching mechanisms of emission B

The temperature-intensity plots in figures 11 and 12 once more emphasise the relation between the quenching of $(^3H_6,t_{2g})_{S=3/2}\rightarrow{}^2F_{7/2}$ emission B and the subsequent feeding and intensification of $^2F_{5/2}\rightarrow{}^2F_{7/2}$

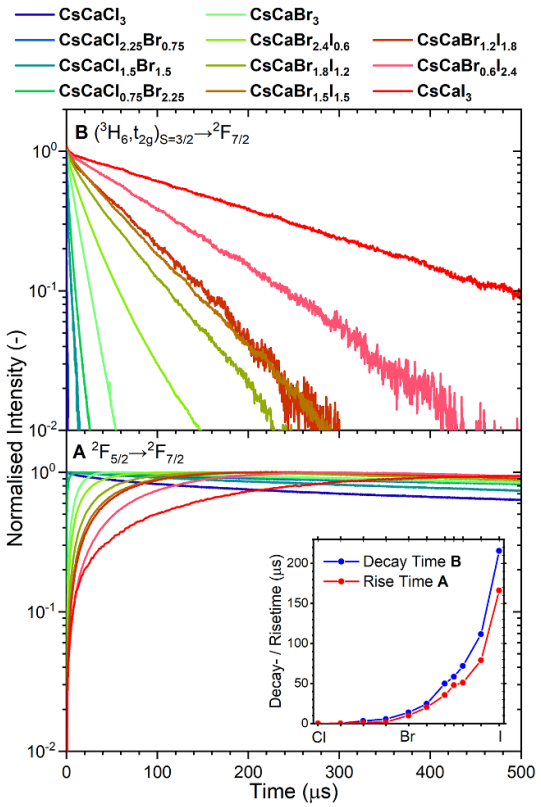

Figure 9. Room temperature decay curves of $(^3H_6,t_{2g})_{S=3/2}\rightarrow{}^2F_{7/2}$ emission B (top) and $^2F_{5/2}\rightarrow{}^2F_{7/2}$ emission A (bottom) after laser excitation into the $(^3H_6,t_{2g})_{S=1/2}$ levels. The curves of emission A display a clear risetime phenomena. The inset shows that its duration is close to the decay time of emission B.

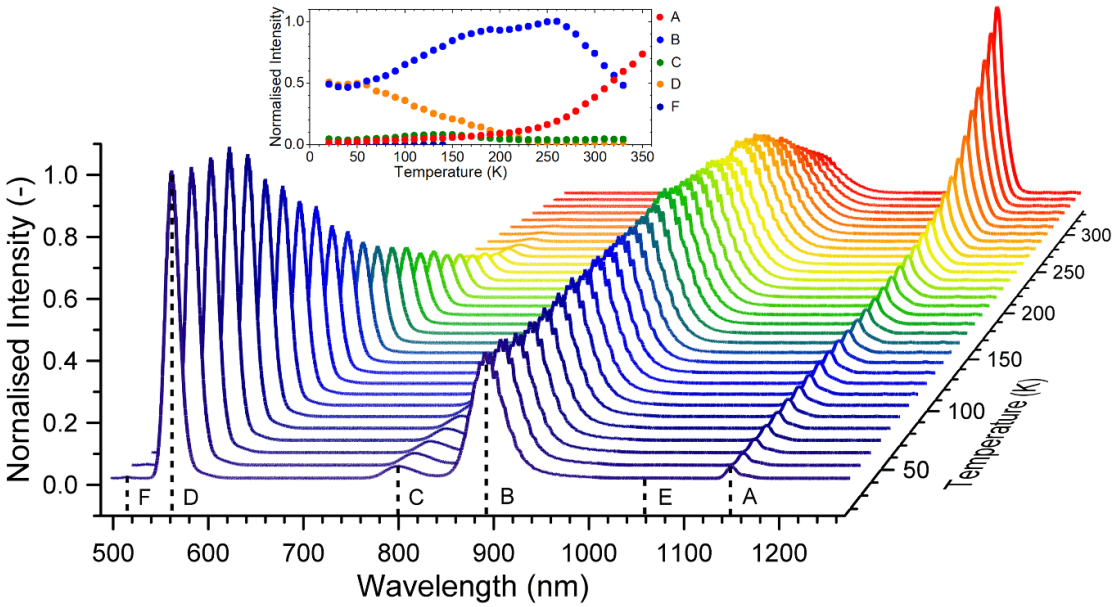

Figure 10. 3D-Plot showing the qualitative behaviour of the six Tm^{2+} emissions (A–F) in $CsCaI_3:Tm^{2+}$ over temperature. The complementary inset presents the integrated luminescence signals over temperature and allows for a qualitative description of the observed trends. The spectra are corrected for the sensitivity of detection and normalised on the $(^3F_4,t_{2g})_{S=3/2}\rightarrow{}^2F_{7/2}$ emission D at 20 K. Photoexcitation occurred into the $(^3F_4,t_{2g})_{S=1/2}$ levels at 455 nm.

emission A. In case of $CsCaBr_3:Tm^{2+}$ and $CsCaI_3:Tm^{2+}$, the relatively strong presence of $(^3H_6,t_{2g})_{S=3/2}\rightarrow{}^2F_{7/2}$ emission C allows for a clear separation with emission B and the integrated intensity curves are added to the plots. As discussed in the previous subsection, emission C rapidly undergoes quenching via MPR and feeds the $(^3H_6,t_{2g})_{S=3/2}$ levels, causing for a slight intensification of emission B.

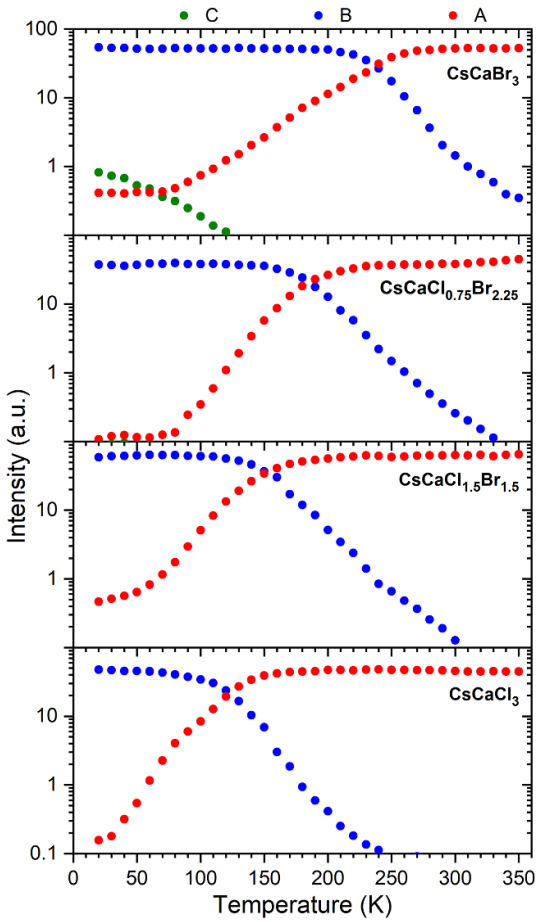

Figure 11. Temperature-intensity plots showing the luminescence behaviour of $^2F_{5/2}\rightarrow{}^2F_{7/2}$ emission A and $(^3H_6,t_{2g})_{S=3/2}\rightarrow{}^2F_{7/2}$ emission B in the $CsCa(Cl/Br)_3:Tm^{2+}$ samples over temperature. The relatively strong presence of $(^3H_6,t_{2g})_{S=1/2}\rightarrow{}^2F_{7/2}$ emission C in $CsCaBr_3:Tm^{2+}$ enabled it to be monitored over temperature and included in the figure. The curves are corrected for the sensitivity of detection and scaled on the QE of $^2F_{5/2}\rightarrow{}^2F_{7/2}$ emission A at room temperature. Photoexcitation occurred into the $(^3H_6,t_{2g})_{S=1/2}$ levels.

For emission B, the temperature onset of the quenching undergoes a clear shift towards higher temperatures when traversing from Cl→Br→I. This, despite the fact that the energy gap between the $(^3H_6,t_{2g})_{S=3/2}$ and $^2F_{5/2}$ levels decreases along the series, from around 3610 to 2560 cm^{-1}, and a significant increase of the related Stokes shift, from around 824 to 1015 cm^{-1}, which presumes a larger configuration displacement between the two levels. Besides, the drop-off in the intensity curves of emission B in figures 11 and 12 becomes less steep from Cl→Br→I and the retrieved Arrhenius deactivation energies increase. Furthermore, the temperature at which the intensity of emission B has reached half of its original value, referred to as $T_{50\%}$, also shifts to higher values. An overview plot of the trends among these parameters, as a function of the Br/Cl and Br/I ratios in the samples, is provided in figure 13 with their values listed in table S4 in the SI.

3.4.2. IC

The quenching of emission B involves a non-radiative $4f^{12}5d^1\rightarrow4f^{13}$ transition that can take place via IC. This quenching mechanism involves the crossing point between the parabolas representing the $(^3H_6,t_{2g})_{S=3/2}$ and $^2F_{5/2}$ states, which can be visualised in a CCD. Section 7.6 of the SI provides additional background information on this topic [34, 35]. The gathered data in tables S2 and S4 in the SI provides the input to draw the CCDs displayed in figure 14. These diagrams immediately reveal that the IC energy barrier ε, associated with the crossing point, is to large extent dependent upon the Stokes shift of the $(^3H_6,t_{2g})_{S=3/2}\rightarrow{}^2F_{7/2}$ emission and the energy gap between the $(^3H_6,t_{2g})_{S=3/2}$ and $^2F_{5/2}$ states. As the related Stokes shift increases from Cl→Br→I and the energy gap becomes smaller, the IC energy barrier will decrease from Cl→Br→I. The crossing point will therefore be situated at lowest energy for $CsCaI_3:Tm^{2+}$, followed by $CsCaBr_3:Tm^{2+}$ and lastly $CsCaCl_3:Tm^{2+}$. Emission B is then predicted to undergo quenching in the order of I→Br→Cl. However, this order does not match the trend of the retrieved Arrhenius deactivation energies and figures 11 and 12 portray an exact opposite quenching behaviour from Cl→Br→I.

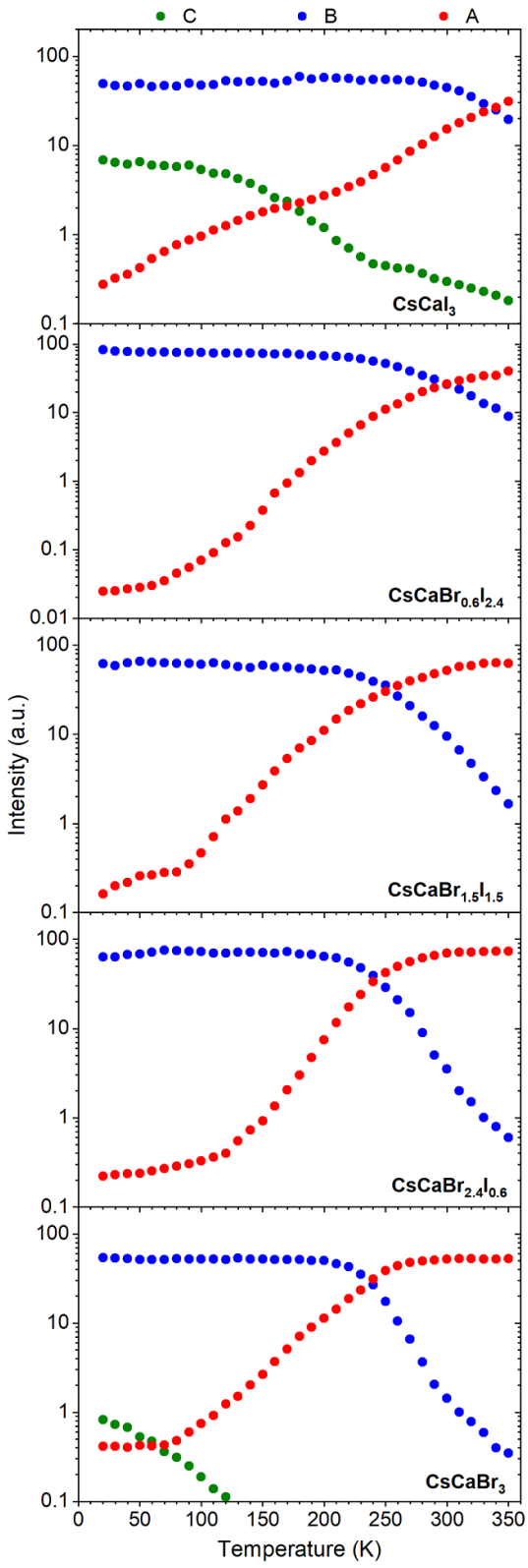

Figure 12. Temperature-intensity plots analogous to figure 11, but related to the $CsCa(Br/I)_3:Tm^{2+}$ samples.

Previously, Koster *et al* [36] used a basic fitting routine to describe the quenching of emission B, in $CsCaCl_3:Tm^{2+}$ and $CsCaBr_3:Tm^{2+}$, via IC by fitting its luminescence lifetime over temperature. It was suggested that the related IC energy barrier in $CsCaCl_3:Tm^{2+}$ could be much smaller than that in $CsCaBr_3:Tm^{2+}$. The interpretation of our data, however, suggests that the barrier in $CsCaCl_3:Tm^{2+}$ is larger than in $CsCaBr_3:Tm^{2+}$.

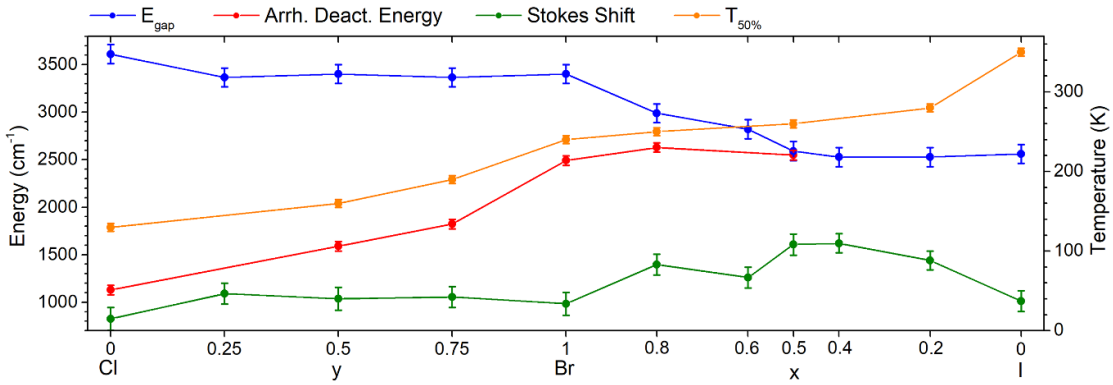

Figure 13. Diagram showing the behaviour of important $(^3H_6,t_{2g})_{S=3/2}$-$^2F_{5/2}$ quenching parameters as plotted versus the Br/Cl and Br/I ratios in the samples. Displayed are: the energy gap E_{gap} between the $(^3H_6,t_{2g})_{S=3/2}$ and $^2F_{5/2}$ levels, the Stokes shift and the Arrhenius deactivation energy and $T_{50\%}$ of the $(^3H_6,t_{2g})_{S=3/2}\rightarrow{}^2F_{7/2}$ emission. Values are provided in table S2 in the SI.

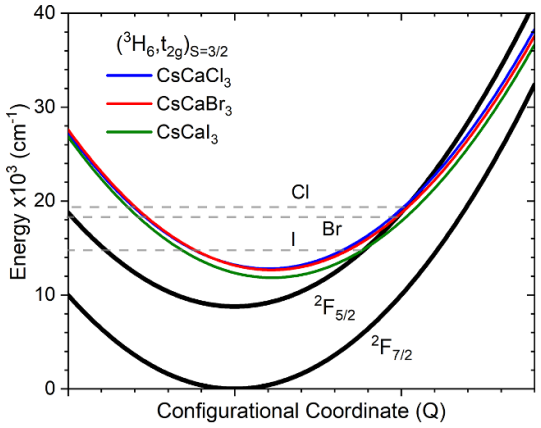

Figure 14. Configurational coordinate diagram revealing the Tm^{2+} $^2F_{5/2}$, $^2F_{5/2}$ and $(^3H_6,t_{2g})_{S=3/2}$ state parabolas. The latter ones are drawn for $CsCaX_3$:Tm^{2+} (X = Cl, Br, I) using the information in section 7.6 of the SI. Note: all state parabolas are drawn here with equal elastic force constant.

The non-radiative transition rate related to the process of IC is governed by the relation: $W = s \cdot e^{-\varepsilon/kT}$ [20, 37]. In this relation: k is the Boltzmann constant, T represents temperature and s is a constant that represents the product of the transition probability between the $(^3H_6,t_{2g})_{S=3/2}$ and $^2F_{5/2}$ states and a frequency with which the excited state reaches the intersection point. This latter constant is weakly dependent upon temperature [37]. A mathematical interpretation of the non-radiative transition rate W in relation to the intensity curves of emission B in figures 11 and 12, shows that the onset of the quenching would be governed by s while the slope of the intensity curve is determined by ε and hence linked to the Arrhenius deactivation energy. Although the onset of the quenching of emission B could be explained by a different value for s, there is still a mismatch in trends between the IC energy barrier ε and the Arrhenius deactivation energy E_{deact}. This does not enable it to couple the quenching of emission B to the process of IC. Nevertheless it is still possible that this process is triggered at higher temperatures. This was also the case in our recent study [9], where we investigated the quenching of emission B in $CaBr_2$:Tm^{2+} via numerical modelling of the non-radiative relaxation rates of IC and MPR.

3.4.3. MPR

The quenching of $4f^{12}5d^1\rightarrow4f^{13}$ emission B can also occur via MPR. This mechanism was previously opted by Grimm and Beurer *et al* [12–14]. However, in these studies the energy gaps between the $(^3H_6,t_{2g})_{S=3/2}$ and $^2F_{5/2}$ levels was determined from absorption spectra and amounted to 2760, 2620 and 2700 cm^{-1} for $CsCaCl_3$:Tm^{2+}, $CsCaBr_3$:Tm^{2+} and $CsCaI_3$:Tm^{2+} respectively. The required amount of vibrational quanta to bridge these gaps were respectively calculated on 9, 13 and 16 quanta. This would mean that emission B undergoes quenching in the order of Cl→Br→I, which is exactly what is observed in figures 11 and 12. However, as the $(^3H_6,t_{2g})_{S=3/2}$ and $^2F_{5/2}$ levels are shifted in configurational coordinates, the energy gaps are more accurately determined from a subtraction of the $(^3H_6,t_{2g})_{S=3/2}\rightarrow{}^2F_{7/2}$ and $^2F_{5/2}\rightarrow{}^2F_{7/2}$ emission

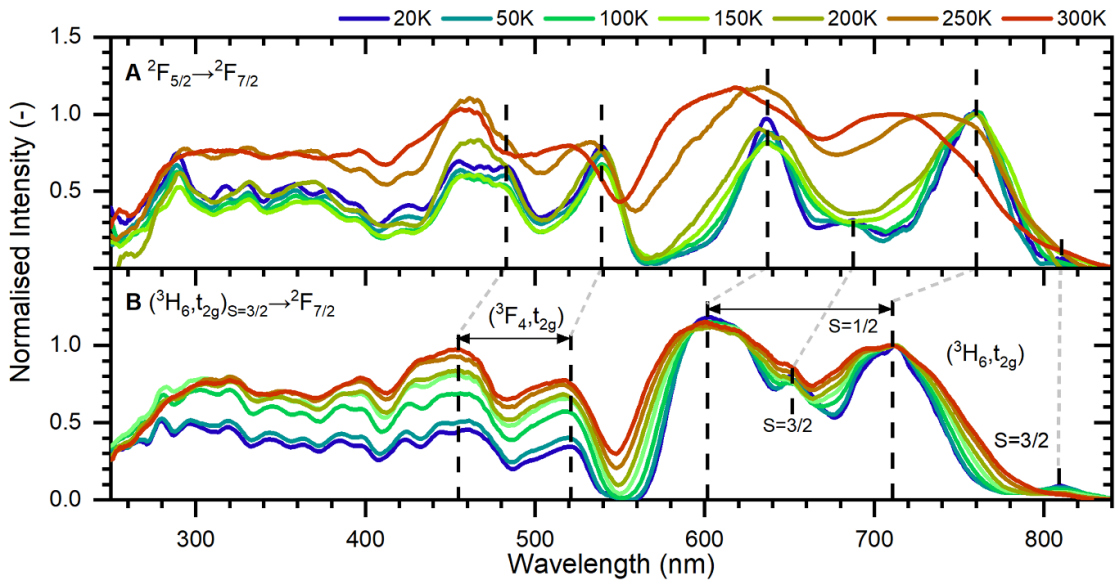

Figure 15. Excitation spectra as acquired on $^2F_{5/2}\rightarrow{}^2F_{7/2}$ emission A and $(^3H_6,t_{2g})_{S=3/2}\rightarrow{}^2F_{7/2}$ emission B in $CsCaI_3:Tm^{2+}$ at various temperatures. The lowest energy $4f^{12}5d^1$ levels are indicated in the figure. Normalisation occurred on the $(^3H_6,t_{2g})_{S=1/2}$ band at longer wavelength (710–780 nm).

energies. If we perform such a calculation based on figure 6, the energy gaps for $CsCaCl_3:Tm^{2+}$, $CsCaBr_3:Tm^{2+}$ and $CsCaI_3:Tm^{2+}$ respectively amount to around 3610, 3400 and 2560 cm^{-1}. Upon using the same phonon energies reported by Grimm *et al* [6], the gaps respectively resemble 12, 16, and 15 vibrational quanta. In this sense, emission B would be expected to quench first in $CsCaCl_3:Tm^{2+}$ and at almost equal temperature in $CsCaBr_3:Tm^{2+}$ and $CsCaI_3:Tm^{2+}$. Figures 11 and 12 show that emission B indeed quenches first in $CsCaCl_3:Tm^{2+}$ and then in $CsCaBr_3:Tm^{2+}$. However, it quenches at a much higher temperature for $CsCaI_3:Tm^{2+}$. Nevertheless, the calculated energy gap and required amount of phonons, as determined using our approach, are quite close to those found in the excited states absorption study by Karbowiak *et al* [38]. As the quenching involves a $4f^{12}5d^1\rightarrow4f^{12}$ transition, and not a $4f^{x-1}5d^1\rightarrow4f^{x-1}5d^1$ or textbook $4f^x\rightarrow4f^x$ transition, the electron–phonon coupling will be stronger. From Moos *et al* [39] it follows that for $4f^x\rightarrow4f^x$ transitions of Nd^{3+}, Dy^{3+} and Ho^{3+} in LaX_3 (X = F, Cl, Br), the coupling constant increases with the size of the crystal field splitting. This is confirmed also in a study by Riseberg *et al* [40] on similar materials. It is thus very likely that the electron–phonon coupling is weaker in $CsCaI_3:Tm^{2+}$ than in, for instance, $CsCaBr_3:Tm^{2+}$ and hence more phonons would be required to bridge the gap between the $(^3H_6,t_{2g})_{S=3/2}$ and $^2F_{5/2}$ levels. This would result in a higher quenching temperature for emission B in $CsCaI_3:Tm^{2+}$, as compared to for instance $CsCaBr_3:Tm^{2+}$, and could hence perhaps explain the observed trends in figures 11 and 12.

3.4.4. Temperature-dependent excitation spectra

As the quenching mechanism related to emission B is perhaps explained by MPR and different electron–phonon coupling constants, we have decided to extend the investigation by studying the temperature-dependent excitation spectra of $^2F_{5/2}\rightarrow{}^2F_{7/2}$ emission A and $(^3H_6,t_{2g})_{S=3/2}\rightarrow{}^2F_{7/2}$ emission B in $CsCaI_3:Tm^{2+}$. Figure 15 shows these temperature-dependent excitation spectra as normalised on the $(^3H_6,t_{2g})_{S=1/2}$ band at longer wavelength. The excitation spectra acquired on emission B (lower panel) reveal that the intensity of the $(^3F_4,t_{2g})$ and higher energy levels undergo a relative increase over temperature, as compared to the $(^3H_6,t_{2g})$ levels. This can be explained by the fact that excitation into the $(^3F_4,t_{2g})$ levels at low temperature results predominantly in $(^3F_4,t_{2g})_{S=3/2}\rightarrow{}^2F_{7/2}$ emission D, and not in $(^3H_6,t_{2g})_{S=3/2}\rightarrow{}^2F_{7/2}$ emission B. As the temperature increases, emission D undergoes quenching and feeds the $(^3H_6,t_{2g})$ levels from which emissions B and C occur. However, this feeding will primarily result into emission B, because $(^3H_6,t_{2g})_{S=1/2}\rightarrow{}^2F_{7/2}$ emission C already starts to quench at 20 K. Besides, a direct excitation in the $(^3H_6,t_{2g})$ levels will, at all temperatures, result primarily in emission B. The excitation spectra thus confirm the sequential feeding route from $(^3F_4,t_{2g})_{S=3/2}\rightarrow(^3H_6,t_{2g})_{S=1/2}\rightarrow(^3H_6,t_{2g})_{S=3/2}$. A comparison between the spectra acquired on emission A (top panel) and B (lower panel), reveals that between 20 K and 200 K there is a significant difference in energy and shape of the excitation bands. As the temperature increases to above 250 K, the excitation bands that result in emission A start to broaden-up and shift in energy in such a way that at 300 K the spectra monitoring emission A and B are almost identical.

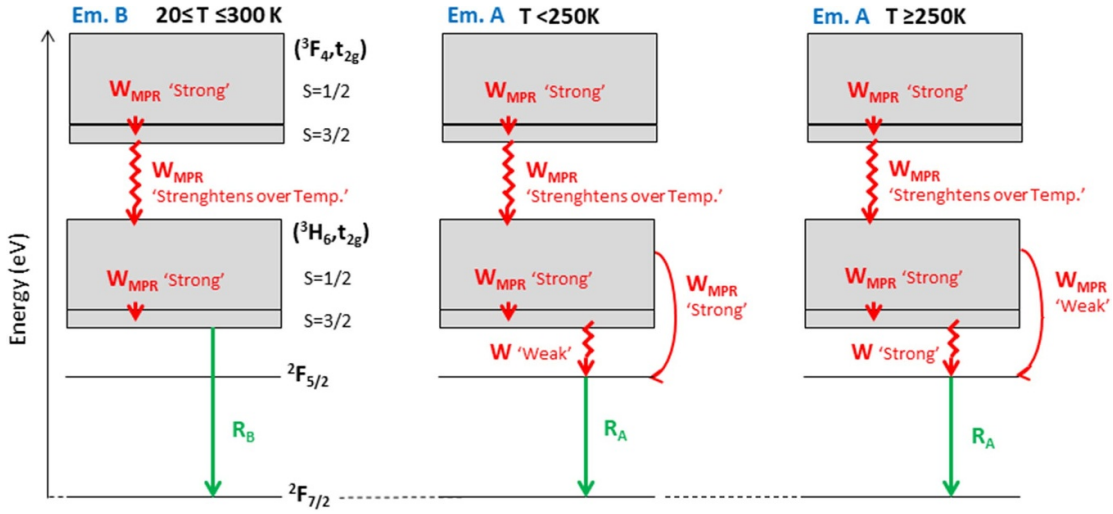

Figure 16. Possible explanation for the different excitation spectra as observed in figure 15. The left diagram explains the excitation spectra observed for $(^3H_6,t_{2g})_{S=3/2}\rightarrow{}^2F_{7/2}$ emission B at $20 \leqslant T \leqslant 300$ K. The central diagram explains the excitation spectra of $^2F_{5/2}\rightarrow{}^2F_{7/2}$ emission A at $T < 250$ K using a strong W_{MPR} feeding from the $(^3H_6,t_{2g})_{S=1/2}$ levels to the $^2F_{5/2}$ level, whereas the right diagram explains this situation at $T \geqslant 250$ K.

One explanation for this peculiar observation could be the presence of two luminescent Tm^{2+} sites in the material: a 'dominant' site and a 'minority' site. The Tm^{2+} ions that occupy the 'minority' site are responsible for the weak presence of $4f^{13}\rightarrow4f^{13}$ emission A at low temperature. As these Tm^{2+} ions have a different anion coordination geometry and undergo a large crystal field splitting, a different excitation spectrum is witnessed in figure 15. When the temperature increases to 250 K, $4f^{12}5d^1\rightarrow4f^{13}$ emission B from the 'dominant' site starts to quench and, consequently, the intensity of $4f^{13}\rightarrow4f^{13}$ emission A from the 'dominant' site increases. It becomes typically a 100× stronger in intensity as compared to emission A from the 'minority' site, which is only visible at low temperature when emission A from the 'dominant' site has no intensity. For temperatures above 250 K, the excitation spectra of emission A now resembles that of the 'dominant' site. The Tm^{2+} ions that occupy this site undergo a smaller crystal field splitting as compared to the 'minority' site. Nevertheless, the Rietveld refinement revealed the presence of a single phase for $CsCaI_3$:Tm^{2+} and also our emission spectra give no hints for the presence of two sites that for example would display multiple emission bands at different energies.

Alternatively, the change in shape of the $4f^{13}\rightarrow4f^{13}$ excitation spectra could perhaps be explained via different thermally activated non-radiative relaxation routes, as illustrated by the schematics in figure 16. Already at low temperature, the excitation spectra as acquired on $^2F_{5/2}\rightarrow{}^2F_{7/2}$ emission A reveal the presence of the $(^3H_6,t_{2g})_{S=3/2}$ levels. It indicates a low temperature relaxation route from the $(^3H_6,t_{2g})_{S=3/2}$ levels to the $^2F_{5/2}$ level. However, the temperature-dependent emission spectra in figure 10 reveal that $(^3H_6,t_{2g})_{S=3/2}\rightarrow{}^2F_{7/2}$ emission B is very intense at these temperatures. It could therefore be that the $^2F_{5/2}$ level is fed via a different non-radiative relaxation route. In our previous work on CaX_2:Tm^{2+} (X = Cl, Br, I) we came to a similar interpretation [20]. There the low-temperature risetime phenomena in the decay curves of emission A showed a clear discrepancy in timing with the luminescence lifetime of emission B. As the temperature increased, the duration of the risetime increased as well and started to converge to the lifetime measured for emission B. It was proposed that at low temperature, a feeding via MPR occurs from the $(^3H_6,t_{2g})_{S=1/2}$ levels to the $^2F_{5/2}$ level. In case of such a $(^3H_6,t_{2g})_{S=1/2}\rightarrow{}^2F_{5/2}$ relaxation route, it is likely that certain $4f^{12}5d^1$ levels within the $(^3H_6,t_{2g})_{S=1/2}$ bands have a relatively stronger or weaker feeding contribution to the $^2F_{5/2}$ level as compared to the $(^3H_6,t_{2g})_{S=1/2}\rightarrow(^3H_6,t_{2g})_{S=3/2}\rightarrow{}^2F_{5/2}$ relaxation route. If we assume the $(^3H_6,t_{2g})_{S=1/2}\rightarrow{}^2F_{5/2}$ route to be dominant at low temperature, the excitation spectra as acquired on $^2F_{5/2}\rightarrow{}^2F_{7/2}$ emission A could have a different shape. With the profound quenching of $(^3H_6,t_{2g})_{S=3/2}\rightarrow{}^2F_{7/2}$ emission B at 250 K, the $(^3H_6,t_{2g})_{S=3/2}\rightarrow{}^2F_{5/2}$ relaxation route is likely to become the dominant $^2F_{5/2}$ feeding route. The excitation spectra as acquired on emissions A and B would then have a similar shape.

4. Summary and conclusions

In this study we systematically vary the Cl/Br and Br/I ratios in $CsCaX_3$:Tm^{2+} (X = Cl, Br, I) compounds. A structural analysis reveals that the samples exhibit the cubic $CaTiO_3$ perovskite structure, with space group $Pm\bar{3}m$, from $CsCaCl_3$ up to $CsCaBr_{1.5}I_{1.5}$. As the Br/I ratio is increased further, the lattice of the $CsCaBr_{1.2}I_{1.8}$

and $CsCaBr_{0.6}I_{2.4}$ samples adopts the tetragonal $NaNbO_3$ structure with space group $P4/mbm$. The CaX_6 octahedra are now rotated around the crystallographic c-axis. For $CsCaI_3$ the crystal structure finally changes into the orthorhombic $GdFeO_3$ structure with space group $Pbnm$, where the octahedra are both rotated around the c-axis and titled. In all cases, the Tm^{2+} ions occupy the Ca^{2+}-site and exhibit a six-fold octahedral coordination geometry.

Excitation spectra acquired on the Tm^{2+} $^2F_{5/2}\rightarrow{}^2F_{7/2}$ and $(^3H_6,t_{2g})_{S=3/2}\rightarrow{}^2F_{7/2}$ emissions in the samples, reveal that the $4f^{12}5d^1$ $(^3F_4,t_{2g})$ and $(^3H_6,t_{2g})$ levels gradually shift towards longer wavelengths for Cl→Br→I. As a result, the energy gap between the $4f^{12}5d^1$ $(^3H_6,t_{2g})_{S=3/2}$ and the $4f^{13}$ $^2F_{5/2}$ levels becomes smaller. The low temperature emission spectra reveal up to six distinct Tm^{2+} emissions. These emissions also undergo a shift towards longer wavelengths for Cl→Br→I. Moreover, the Stokes shifts between the absorption and emission increases. As the temperature rises, the various $4f^{12}5d^1\rightarrow4f^{13}$ emissions undergo quenching. As the configurational displacement between the $4f^{12}5d^1$ levels is negligible, most of the $4f^{12}5d^1\rightarrow4f^{13}$ emissions will quench via MPR. In case of the lowest energy $4f^{12}5d^1\rightarrow4f^{13}$ emission, the quenching can occur via MPR and/or IC. Temperature-intensity plots reveal that the temperature onset of the quenching of this $(^3H_6,t_{2g})_{S=3/2}\rightarrow{}^2F_{7/2}$ emission gradually shifts towards higher temperatures when traversing from Cl→Br→I. In addition, the Arrhenius deactivation energy increases from Cl→Br→I. This is contrary to our expectation as the energy gap between the $(^3H_6,t_{2g})_{S=3/2}$ and $^2F_{5/2}$ levels decreases along the series. An analysis reveals that the process of IC is unable to explain the quenching of the $(^3H_6,t_{2g})_{S=3/2}\rightarrow{}^2F_{7/2}$ emission, as the energy gap and Stokes shift predict it to quenching in the order I→Br→Cl. In case of MPR, the required amount of phonons to bridge the energy gap in $CsCaCl_3$:Tm^{2+} is smaller than in $CsCaBr_3$:Tm^{2+}, and about equal for $CsCaBr_3$:Tm^{2+} and $CsCaI_3$:Tm^{2+}. A decrease of the electron–phonon coupling strength in the direction Cl→Br→I could explain the observed quenching trend in the samples. This would entail an additional, required, amount of phonons to activate the quenching in $CsCaI_3$:Tm^{2+}. However, no such information is available from literature. It would request a detailed investigation of how the vibrational modes of the host couple to the electronic states of Tm^{2+}.

An additional investigation into the temperature-dependent excitation spectra of the $^2F_{5/2}\rightarrow{}^2F_{7/2}$ and $(^3H_6,t_{2g})_{S=3/2}\rightarrow{}^2F_{7/2}$ emissions reveals a peculiar difference in the shape of the spectra. This difference is observed at temperatures where the $^2F_{5/2}\rightarrow{}^2F_{7/2}$ emission intensity is weak and almost independent of temperature. However, the $^2F_{5/2}\rightarrow{}^2F_{7/2}$ and $(^3H_6,t_{2g})_{S=3/2}\rightarrow{}^2F_{7/2}$ emission intensities display a clear anti-correlated trend in both time and temperature for all of the studied compounds. This anti-correlation is also observed in the measured QEs. When traversing from Br→I, the QE of the $^2F_{5/2}\rightarrow{}^2F_{7/2}$ emission decreases from around 70% to 15%, while the QE of the $(^3H_6,t_{2g})_{S=3/2}\rightarrow{}^2F_{7/2}$ emission increases to around 45%. However, large random fluctuations, of several tens of per cent, are observed among the measured QEs. This makes us believe that the QE is largely governed by defects, such as vacancies, that are present in the materials. Without them, the QE can approach 100%, as no non-radiative relaxation routes to the ground state have been identified.

Data availability statement

The data generated and/or analysed during the current study are not publicly available for legal/ethical reasons but are available from the corresponding author on reasonable request.

Acknowledgment

This research was financially supported by the Nederlandse Organisatie voor Wetenschappelijk onderzoek (NWO) - Toegepaste Technische Wetenschappen (TTW) LumiCon Project Grant No 15024 as part of the LumiCon proposal. The authors would like to thank J T M de Haas (TU Delft) for overall support with the photoluminescence setups. In addition, C van Aarle and V Khanin are thanked for fruitful discussion on the results.

ORCID iD

M P Plokker https://orcid.org/0000-0002-1939-0649

References

[1] Mathur A, Fan H and Maheshwari V 2021 Organolead halide perovskites beyond solar cells: self-powered devices and the associated progress and challenges *Mater. Adv.* **2** 5274–99

[2] Kim H-S, Im S H and Park N-G 2014 Organolead halide perovskite: new horizons in solar cell research *J. Phys. Chem.* C **118** 5615–25
[3] Su L, Zhao Z X, Li H Y, Yuan J, Wang Z L, Cao G Z and Zhu G 2015 High-performance organolead halide perovskite-based self-powered triboelectric photodetector *ACS Nano* **9** 11310–6
[4] Awater R H P and Dorenbos P 2017 The vacuum referred electron binding energies in the $^1S_0$ and $^3P_1$ states of Pb^{2+} and Tl^{+} in inorganic compounds *J. Lumin.* **192** 783–93
[5] Suta M, Urland W, Daul C and Wickleder C 2016 Photoluminescence properties of Yb^{2+} ions doped in the perovskites $CsCaX_3$ and $CsSrX_3$ (X = Cl, Br, and I)—a comparative study *Phys. Chem. Chem. Phys.* **18** 13196
[6] Suta M, Larsen P, Lavoie-Cardinal F and Wickleder C 2014 Photoluminescence of $CsMBr_3$:Eu^{2+} (M = Mg, Ca, Sr)—a novel strategy for the development of low-energy emitting phosphors *J. Lumin.* **149** 35–44
[7] Suta M and Wickleder C 2017 Spin crossover of Yb^{2+} in $CsCaX_3$ and $CsSrX_3$ (X = Cl, Br, I)—a guideline to novel halide-based scintillators *Adv. Funct. Mater.* **27** 1602783
[8] Suta M, Senden T, Olchowka J, Adlung M, Meijerink A and Wickleder C 2017 Decay times of the spin-forbidden and spin-enabled transitions of Yb^{2+} doped in $CsCaX_3$ and $CsSrX_3$ (X = Cl, Br, I) *Phys. Chem. Chem. Phys.* **19** 7188
[9] Lindsey A, McAlexander W, Stand L, Wu Y, Zhuravleva M and Melcher C L 2015 Crystal growth and spectroscopic performance of large crystalline boules of $CsCaI_3$: Eu scintillator *J. Cryst. Growth* **427** 42–47
[10] Loyd M, Lindsey A, Patel M, Koschan M, Melcher C L and Zhuravleva M 2018 Crystal structure and thermal expansion of $CsCaI_3$:Eu and $CsSrBr_3$:Eu scintillators *J. Cryst. Growth* **481** 35–30
[11] Loyd M, Lindsey A, Stand L, Zhuravleva M, Melcher C L and Koschan M 2017 Tuning the structure of $CsCaI_3$:Eu via substitution of bromine for iodine *Opt. Mater.* **68** 47–52
[12] Grimm J and Güdel H U 2005 Five different types of spontaneous emission simultaneously observed in Tm^{2+} doped $CsCaBr_3$ *Chem. Phys. Lett.* **404** 40–43
[13] Grimm J, Suyver J F, Carver G and Güdel H U 2006 Light-emission and excited-state dynamics in Tm^{2+} doped $CsCal_3$, $CsCaBr_3$, and $CsCaI_3$ *J. Phys. Chem.* B **110** 2093–101
[14] Beurer E, Grimm J, Gerner P and Güdel H U 2006 Absorption, light emission, and upconversion properties of Tm^{2+}-doped $CsCaI_3$ and $RbCaI_3$ *Inorg. Chem.* **45** 9901–6
[15] Grimm J, Beurer E and Güdel H U 2006 Crystal absorption spectra in the region of 4f-4f and 4f-5d excitations in Tm^{2+}-doped $CsCaCl_3$, $CsCaBr_3$, and $CsCaI_3$ *Inorg. Chem.* **45** 10905–8
[16] Beurer E, Grimm J, Gerner P and Güdel H U 2006 New type of near-infrared to visible photon upconversion in Tm^{2+}-doped $CsCaI_3$ *J. Am. Chem. Soc.* **128** 3110–1
[17] Grimm J, Beurer E, Gerner P and Güdel H U 2007 Upconversion between 4f–5d excited states in Tm^{2+}-doped $CsCaCl_3$, $CsCaBr_3$, and $CsCaI_3$ *Chem. Eur. J.* **13** 1152–7
[18] de Jong M, Biner D, Krämer K W, Barandiarán Z, Seijo L and Meijerink A 2016 New insights in $4f^{12}5d^1$ excited states of Tm^{2+} through excited state excitation spectroscopy *J. Phys. Chem. Lett.* **7** 2730–4
[19] de Jong M, Meijerink A, Seijo L and Barandiarán Z 2017 Energy level structure and multiple $4f^{12}5d^1$ emission bands for Tm^{2+} in halide perovskites: theory and experiment *J. Phys. Chem.* C **121** 10095–101
[20] Plokker M P, van der Knijff I C, de Wit A V, Voet B, Woudstra T, Khanin V, Dorenbos P and van der Kolk E 2021 Experimental and numerical analysis of Tm^{2+} excited-states dynamics and luminescence in CaX_2 (X = Cl, Br, I) *J. Phys.: Condens. Matter* **33** 255701
[21] Ten Kate O M, Krämer K W and van der Kolk E 2015 Efficient luminescent solar concentrators based on self-absorption free, Tm^{2+} doped halides *Sol. Energy Mater. Sol. Cells* **140** 115–20
[22] Rodriguez-Carvajal J Program FullProf.2k, version 5.2 July 2011 Institute Laue Langevin
[23] Rogers E, Dorenbos P, de Haas J T M and van der Kolk E 2012 Experimental study of the $4f^n \rightarrow 4f^n$ and $4f^n \rightarrow 4f^{n-1}5d^1$ transitions of the lanthanide diiodides LnI_2 (Ln = Nd, Sm, Eu, Dy, Tm, Yb) *J. Phys.: Condens. Matter* **24** 275502
[24] National Bureau of Standards 1967 NBS Monograph **25** 21
[25] Seifert H J and Habenauer D 1982 *Z. Anorg. Allg. Chem.* **301** 491
[26] Schilling G, Kunert C, Schleid T H and Meyer G 1992 Metallothermische reduktion der tribromide und -iodide von thulium und ytterbium mit alkalimetallen *Z. Anorg. Allg. Chem.* **7** 618
[27] Hohnstedt C and Meyer G 1993 Metallothermische reduktion des tribromids und -iodids von dysprosium mit alkalimetallen *Z. Anorg. Allg. Chem.* **619** 1374
[28] Schilling G and Meyer G 1996 Ternäre bromide und iodide zweiwertiger lanthanide und ihre erdalkali-analoga vom Typ AMX_3 und AM_2X_5 *Z. Anorg. Allg. Chem.* **622** 759
[29] Dieke G H and Crosswhite H M 1963 The spectra of the doubly and triply ionized rare earths *Appl. Opt.* **2** 675–86
[30] Plokker M P and van der Kolk E 2019 Temperature dependent relaxation dynamics of luminescent NaX:Tm^{2+} (X = Cl, Br, I) *J. Lumin.* **216** 116694
[31] Plokker M P, Hoogsteen W, Abellon R D, Krämer K W and van der Kolk E 2020 Concentration and temperature dependent luminescence properties of the SrI_2-TmI_2 system *J. Lumin.* **225** 117327
[32] Dorenbos P 2013 Ce^{3+} 5d-centroid shift and vacuum referred 4f-electron binding energies of all lanthanide impurities in 150 different compounds *J. Lumin.* **93** 135
[33] Dorenbos P 2002 Crystal field splitting of lanthanide $4f^{n-1}5^d$-levels in inorganic compounds *J. Alloys Compd.* **341** 156
[34] Struck C W and Fonger W H 1991 Introduction *Understanding Luminescence Spectra and Efficiency Using Wp and Related Functions* Inorg. Chem. Concepts vol 13 (Berlin: Springer) p 225
[35] Grinberg M and Lesniewski T 2019 Non-radiative processes and luminescence quenching in Mn^{4+} doped phosphors *J. Lumin.* **214** 116574
[36] Koster S, Reid M, Wells J P and Reeves R 2014 Energy levels and dynamics of Tm^{2+} doped into AMX3 salts MSc Thesis (University of Canterbury)
[37] Yen W M, Shionoya S and Yamamoto H 2007 *Phosphor Handbook* 2nd edn (Boca Raton, FL: CRC Press Taylor & Francis Group), ch 2
[38] Karbowiak M, Lisiecki R, Solarz P, Komar J and Ryba-Romanowski W 2018 Spectroscopic peculiarities of $CsCaI_3$:Tm^{2+} single crystals examined through one-photon and excited state excitation spectroscopy *J. Alloys Compd.* **740** 1165–71
[39] Moos H W 1970 Spectroscopic relaxation processes of rare earth ions in crystals *J. Lumin.* **1–2** 106–21
[40] Riseberg L A and Moos H W 1968 Multiphonon orbit-lattice relaxation of excited states of rare-earth ions in crystals *Phys. Rev.* **2** 174